Journal of Materials Chemistry A

PAPER

View Article Online
View Journal | View Issue

Cite this: J. Mater. Chem. A, 2014, 2, 13103

$Co_xMn_{3-x}O_4$ hollow octahedrons: synthesis, growth mechanism, and their application in high-performance supercapacitors

Huang Xiaomin,†[a] Wang Long,†[d] Cao Xia,*[ab] Han Yu,[a] Gao Caizhen,[a] Xu Ying[a] and Wang Ning*[ac]

Received 23rd April 2014
Accepted 12th June 2014

DOI: 10.1039/c4ta02020k

www.rsc.org/MaterialsA

$Co_xMn_{3-x}O_4$ nanorods and hollow octahedrons have been fabricated through a simple hydrothermal method without using any template or surfactant. The growth mechanism is studied by characterizing the intermediate products during the phase transformation. In this strategy, the MnO_2 nanowire serves as the main precursor for the subsequent formation of $Co_xMn_{3-x}O_4$ nanomaterials. A merged dissolution–recrystallization and the Kirkendall effect mechanism has been proposed based on SEM, TEM and XRD characterization of the intermediate. Enhanced specific capacitance (266.84 F g^{-1} at 5 mV s^{-1}), and good cycle stability (remaining 80.214% after 1000 cycles) are observed in aqueous electrolytes, which could be ascribed to the high charge accommodation, small ion-transport resistance, and good electric conductivity.

1 Introduction

Due to increasing demand for energy and depletion of fossil fuels, the development of highly efficient energy storage devices has attracted considerable attention from scientific and technological researchers.[1–3] Implementation of renewable energy sources, such as solar and wind energy, have partially alleviated the pressure on energy demand. Supercapacitors (SCs), also known as electrochemical capacitors, are considered highly efficient storage devices that could bridge the gap between batteries and conventional capacitors due to their high power density, long cycle life, fast charging efficiency, and environmental friendliness.[4–7]

Among the electrode materials with high energy and power densities, ruthenium oxide (RuO_2), which has remarkably high specific capacitance, good proton conductivity, excellent electrochemical reversibility, high rate capability, and long cycle life, has been the most extensively electrode material. However, its lack of abundance, high prices and environmental harmfulness has made it necessary to identify alternative materials for practical applications. Manganese oxides have excellent physical and chemical properties under ambient conditions. In particular, the rich polymorphism and structural flexibility of these compounds make them a good candidate for supercapacitors because of their easy access, low cost, and environmentally friendly nature.[8] Nevertheless, the poor electrical conductivity and significant degradation greatly restrained the realization of their high theoretical capacitances (a theoretical capacity up to 1300 F g^{-1}), especially at high charge/discharge rates in electrochemical cycling, which restricts the research speed of manganese oxides.[9]

The fast development of multidimensional nanomaterials of controllable size, composition, and structure has opened up enormous possibilities for engineering electrode materials with enhanced performance. For example, hollow micro/nanostructured materials have been considered ideal platforms for application in electrochemical energy storage because of their novel interior geometry and shell functionality.[10–14] This kind of structure has increased the contact area between the electrolyte and the active material, and reduced transport lengths for both mass and charge transport. As a result, much effort has been given to synthesize MnO_2-based hollow materials and to develop a rational design to maximize their electrochemically active sites for redox reactions by obtaining "opened" structures to further increase their energy storage density.[15–17]

Moreover, the critical role that impurities/dopants play has stimulated research on the creation of highly conducting nanocrystals.[18–21] Because impurities can be used to alter the properties of nanoscale materials in desirable and controllable ways, doped nanocrystals can address key problems in applications ranging from solar cells to bio-imaging. Highly functional mixed oxide nanocrystals will require improving

[a]Key Laboratory of Bio-Inspired Smart Interfacia Science and Technology of Ministry of Education, School of Chemistry and Environment, Beijing University of Aeronautics and Astronautics, Beijing, 100083, China. E-mail: wangning@buaa.edu.cn; Tel: +86 10 82316688

[b]School of Biochemical and Pharmaceutical Sciences, Capital Medical University, Beijing, 100069, China. E-mail: caoxia@ccmu.edu.cn

[c]Department of Chemistry, Dongguk University, Seoul 100-715, Korea

[d]Department of Equipment Manufacture, Zhongshan Torch Polytechnic, Zhongshan, 528436, China

† These authors contributed equally to this work.

synthetic control over dopant incorporation, optimizing their concentrations, and investigating the phenomena that emerge. However, to the best of our knowledge, the hollow structured mixed manganese oxides have not been used to date as electrode materials for supercapacitors.

In this work, a facile template-free method was developed to synthesise a hollow manganese oxide nanomaterial with tunable morphologies and compositions. Analysis of the intermediate products has proved that hydrothermal treatment of the Co-adsorbed MnO_2 nanowires produced $Co_xMn_{3-x}O_4$ nanorods and hollow octahedrons with tunable compositions. Electrochemical results show that both the energy and the power densities at high rate are greatly improved when the doped manganese oxides are used as the supercapacitor electrode material.

2 Experimental

2.1 Chemicals

All reagents, unless otherwise stated, were purchased from Sinopharm Chemical Reagent Beijing Co. Ltd and used as received without further purification. Deionized water from a Milli-Q system was used throughout the experiments.

2.2 Material synthesis

For the synthesis of cobalt-doped MnO_2 nanowires, $MnCl_2\cdot 4H_2O$ (0.162 g) and $CoCl_2\cdot 6H_2O$ (0.0685 g) were first dissolved in 30 mL of isopropanol with ultrasonication for 30 minutes. After the bright blue solution was heated to 83 °C in a circulating water condenser with vigorous stirring, 30 mL of aqueous $KMnO_4$ solution (containing 0.09 g of $KMnO_4$) was added rapidly. After refluxing for 30 minutes, the mixed product (Intermediate I) was centrifuged, and washed with water and ethanol several times. MnO_2 nanowires were also prepared in a similar way except the addition of $CoCl_2\cdot 6H_2O$. For the synthesis of $Co_xMn_{3-x}O_4$ nanorods and hollow octahedrons, the black slurry in the flask (Intermediate I) was transferred into a 50 mL Teflon-lined stainless steel autoclave and maintained at 200 °C for 2.5 and 5 h, respectively. After cooling to room temperature, the product was washed several times by centrifugation.

2.3 Characterization

High-resolution transmission electron microscopy (HRTEM) images were obtained using a JEM-2010F transmission electron microscope at an acceleration voltage of 200 kV. Scanning electron microscopy (SEM) images were obtained by employing a Hitachi S4800 cold field-emission scanning electron microscope (CFE-SEM). X-ray powder diffraction (XRD) pattern of the samples was obtained by a Rigaku X-ray diffractometer (Rigaku Goniometer PMG-A2, CN2155D2, wavelength = 0.15147 nm) with Cu Kα radiation.

2.4 Electrochemical measurements

All electrochemical experiments were carried out at room temperature using a single compartment, three-electrode cell. An Ag/AgCl electrode was used as the reference electrode, and a Pt wire as the auxiliary electrode. The working electrode was prepared by mixing the 80 wt% of the electro-active material, 10 wt% of carbon black, and 10 wt% of polytetrafluoroethylene emulsion (10%) to obtain well-dispersed ink samples, and then painted on the nickel foam (1 cm^2) and dried at 60 °C for 12 h. Then, all electrodes were pressed into flakes under 10 MPa.

3 Results and discussion

3.1 Structural characterization

SEM images (Fig. 1A and B) show that octahedral manganese oxide particles are synthesized on a large scale and with high uniformity. The octahedrons are enclosed by well-organized facets with an average edge length of about 400 nm and an elongated ⟨001⟩ axe of about 800 nm. Detailed structural information is given by TEM and HRTEM images (Fig. 1C and D). The sharp contrast difference between the center and the edge proves their hollow nature with a wall thickness of about 30 to 50 nm. HRTEM image (Fig. 1D) indicates a typical tetragonal lattice structure, and the marked lattice fringes with a spacing of 0.55 and 0.27 nm, corresponding to the (202) and (311) lattice planes, respectively. Fig. 1E shows the typical XRD pattern of $Co_xMn_{3-x}O_4$. All the diffraction peaks and the high intensity of these peaks indicated the high crystallinity and purity of the $Co_xMn_{3-x}O_4$ product (JCPDS: 18-0410). The energy-dispersive spectrometry (EDS, Fig. 1F and G) result represents an averaged atomic percentage of Co of about 5.7% ($Co_{0.4}Mn_{2.6}O_4$), which can be varied conveniently from 3.8% to 20.6% by changing the precursory cobalt concentrations.

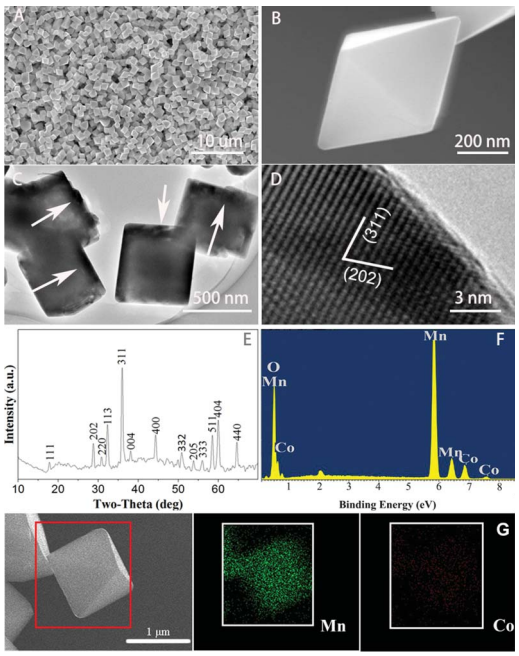

Fig. 1 (A and B) SEM images of $Co_{0.4}Mn_{2.6}O_4$ octahedrons at different magnifications. (C) TEM and (D) HRTEM image of $Co_{0.4}Mn_{2.6}O_4$ octahedrons. (E) XRD pattern and (F) EDS spectra of the $Co_{0.4}Mn_{2.6}O_4$ octahedrons. (G) EDS mapping of the $Co_{0.4}Mn_{2.6}O_4$ octahedrons.

3.2 Growth mechanism

It has been reported that the growth of nanocrystals is rooted in surface energies. The surface energies are usually associated with crystallographic planes and are different in a sequence of $\gamma\{111\} > \gamma\{100\} > \gamma\{110\}$. However, it has also been found that facet-matching may be another driving force for the formation of nanowalls and nanodisks.[22–25] Herein, controlled experiments were carried out to investigate the formation of such hollow octahedrons.

As can be noted from the first step of the synthesis procedure, only $MnCl_2$, $KMnO_4$ and $CoCl_2$ were dissolved and heated at 83 °C and a brown precipitate was obtained. SEM observation proved that ultrathin nanowires were synthesized without using any surfactant (Fig. 2A). XRD characterizations demonstrated the pure phase of MnO_2 (JCPDF no. 44-0141) (Fig. 2F), which indicates that the following chemical reaction was employed.

$$3MnCl_2 + 2KMnO_4 + 2H_2O \rightarrow 5MnO_2\downarrow + 2H_2SO_4 \quad (1)$$

Theoretically, the Gibbs free energy change (2269.2 kJ mol^{-1}) represents a strong tendency for this reaction to progress towards completion. The formation of nanowires is in fact the transformation of manganese hydroxide to oxide, a process that has been well discussed in many publications for the same or similar metal alkoxides;[22–25] *i.e.*, through the formation of Mn–O covalent and Mn–OH coordination bonds, the manganese hydroxide tended to form longer chains and additional one-dimensional nanowires through van der Waals interaction as well as an oxygen-bridge.[19,26] Thus, the MnO_2 nanowires acted as the original material sources for subsequent hydrothermal reactions. In this step, cobalt ion is only adsorbed by the resultant MnO_2 nanowires and does not affect the formation of MnO_2, considering the Gibbs free energy change.

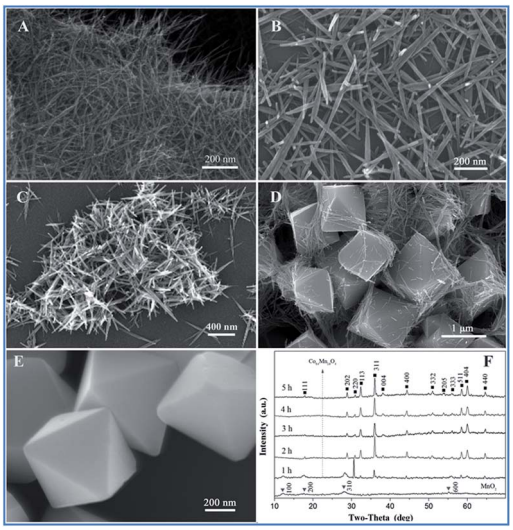

Fig. 2 (A) SEM images of products after step I; (B) products after step II, 1 h; (C) products after step II, 2 h; (D) step II, 4 h; (E) step II, 5 h; (F) comparison of XRD patterns of the product at different reaction times.

In the following hydrothermal step, the morphology changed dramatically from one-dimensional nanowires to hollow-structured octahedrons, which could be ascribed to the dissolution–recrystallization effect under the high reaction temperature and pressure (Fig. 2B–E). It has been reported that the solvothermal reaction can not only promote dissolution of the oxide precursor, but also help to replace hydroxyl groups (OH^-) for oxygen (O^{2-}) and to induce cationic substitutions. Thus, the solubility of the manganese precursor (MnO_2 nanowire) appears to also play an important role for orienting the stabilization of a stable structural form. Here, the stabilization of different structural forms can help form a mixed oxide *via* the following reactions (eqn (2)).

$$6MnO_2 + 3(CH_3)_2CHOH \xrightarrow{\text{hydrothermal}} 2Mn_3O_4 + 3(CH_3)_2CO + 3H_2O \quad (2)$$

$$xCO^{2+} + (3-x)MnO_2 \xrightarrow{\text{hydrothermal}} Co_xMn_{3-x}O_4 \quad (3)$$

The MnO_2 nanowires are first transformed to short $Co_xMn_{3-x}O_4$ nanorods with typical diameters of 20–50 nm and lengths of 200 nm to 1 μm (Fig. 2B), which were then assembled with each other and formed bundle-like aggregates (Fig. 2C). When the reaction further progresses, these shortened nanorods tend to automatically agglomerate together. The obvious dissolution–recrystallization process even caused an interpenetration prototype of octahedrons with a certain angle and contact point, which eventually recrystallized into highly ordered octahedrons (Fig. 2D and E). The phase transformation is also proven by the XRD patterns shown in Fig. 2F. The MnO_2 phase began to diminish with an increase in the reaction time, while the diffraction ascribed to (220) and (311) of $Co_xMn_{3-x}O_4$ intensified gradually. It takes about 2 h for the complete conversion of the cobalt–adsorbed MnO_2 nanowire to $Co_xMn_{3-x}O_4$ nanorods, and 4 h for the Mn_3O_4 nanorod to dissolute and recrystallize into $Co_xMn_{3-x}O_4$ octahedron.

Another interesting issue is the formation mechanism of a hollow structure under hydrothermal conditions. In the past, it has been proposed that manganese oxides develop either from an initial nanoparticle agglomerated mass under the reflux conditions, or a rolling mechanism under the hydrothermal conditions.[27] To investigate the detailed formation process of the hollow structure under hydrothermal conditions, the precipitates were taken out right after the reaction time exceeded 3 h. Note that the reaction does not stop immediately after the autoclave is removed from the heater owing to heat transfer; thus, we can believe that the samples randomly taken represent certain characteristics of the formation process.

Structural information of the as-prepared $Co_xMn_{3-x}O_4$ octahedron was further confirmed by SEM and TEM (Fig. 3). The clearly observed grain boundary within the octahedron hints a mechanism analogous to void formation in the Kirkendall effect (Fig. 3B–E).[28] The two solids (Mn–Co oxides) diffuse into each other at different rates and the unfilled voids are left behind. Within the small volume of a transforming $Co_xMn_{3-x}O_4$ micro/nanocrystal, the supersaturated vacancy

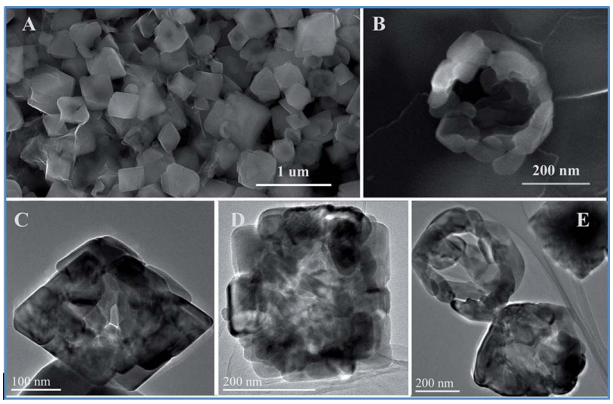

Fig. 3 SEM (A) and TEM (B–E) images of the $Co_xMn_{3-x}O_4$ hollow octahedrons taken from the hydrothermally treated intermediates.

cloud is likely to coalesce into large pores or a single void *via* the following route shown in eqn (3).

For instances of cobalt doping, significant inward cobalt transport could occur through grain boundaries or during the formation of the first few monolayers of $Co_xMn_{3-x}O_4$. It is also possible that inward relaxation of the hole occurs, due to annihilation of vacancies at a semi-coherent or incoherent manganese–cobalt interface (Fig. 3B–E). It is observed that increased cobalt concentration increased the hole size and enhanced the outward growth of the shell, indicating that manganese mobility rather than cobalt mobility was the driving force of formation of inner voids.

We therefore propose a possible growth mechanism for the $Co_xMn_{3-x}O_4$ hollow octahedrons, which can be divided into three stages. Firstly, MnO_2 nanowires are constructed from chains of $\{MnO_6\}$ octahedra, which are linked together to form tunnelled sequences. Under the hydrothermal conditions, dissolution–recrystallization of MnO_2 was initiated for the formation process of $Co_xMn_{3-x}O_4$ nanorods and nano-octahedrons. With the increase of reaction time, the "Ostwald ripening" mechanism became the main factor, which enabled and accelerated the transformation from nanorods to octahedrons to minimize the overall energy of the system. It can be seen that the $Co_xMn_{3-x}O_4$ nanorods are only transient intermediate products. The dissolution of nanorods and the growth of octahedrons almost occur simultaneously under the hydrothermal conditions. Furthermore, increase in the reaction time resulted in CoO-nuclei, which adsorbed on surfaces of Mn_3O_4 octahedrons, forming $Co_xMn_{3-x}O_4$ layers. With the increase in reaction time, the two solids (Mn–Co oxides) diffused into each other at different rates and the unfilled voids are left behind and coalesce into large voids due to the so-called Kirkendall effect. Such process is supported by the morphology evolution at different growth stages by changing the reaction time Fig. 4. The truncated octahedrons results from a much higher growth rate along the ⟨100⟩ direction than the ⟨111⟩ direction due to the lowest energy of the {111} surfaces.

To demonstrate the use of hollow nanocrystals in energy storage, electrochemical performance of the as-synthesized manganese oxides was tested by cyclic voltammetry (CV) at a

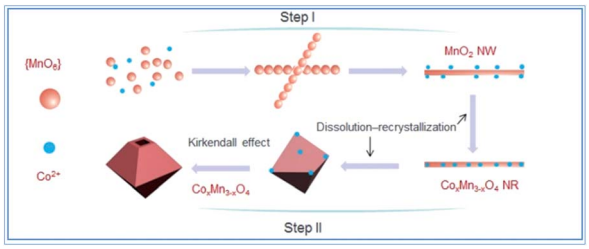

Fig. 4 Schematic illustration of the growth mechanism of the $Co_xMn_{3-x}O_4$ octahedrons.

scan rate of 5 mV s^{-1} in the potential range of 0–1 V using 1 M Na_2SO_4 aqueous electrolyte solution (Fig. 5). The rectangular and symmetric CV curves of MnO_2, Mn_3O_4, and cobalt–adsorbed MnO_2 indicate the typical pseudocapacity, which is in sharp contrast to that of $Co_{0.4}Mn_{2.6}O_4$ and $Co_{1.4}Mn_{1.6}O_4$ (Fig. 5A and B). The lack of symmetry in the latter cases was due to a combination of double-layer and pseudocapacitive effects. In addition, the doped Co ions also make additional contributions to the total capacitance. It is interesting that performances of both $Co_{0.4}Mn_{2.6}O_4$ and $Co_{1.4}Mn_{1.6}O_4$ were significantly improved than that of pure Mn_3O_4 after the hydrothermal treatment, and $Co_{1.4}Mn_{1.6}O_4$ possesses the best performance. Since C_s is proportional to the average areas of CVs compared with that of $Co_{0.4}Mn_{2.6}O_4$ and Mn_3O_4, the average area of $Co_{1.4}Mn_{1.6}O_4$ was almost covered by a straight line at different scan rates, which hints a sound cycling stability and deserves further study. In addition, there appears an anodic peak at around 0.9 V for $Co_{0.4}Mn_{2.6}O_{0.4}$, which should be ascribed to the redox reaction between Mn^{4+} and Mn^{3+}.

Galvanostatic charge/discharge measurements were carried out in 1 M Na_2SO_4 between 0 and 1 V at a current density of 200 mA g^{-1} (Fig. 6). As illustrated in Fig. 6A, during the charging and discharging steps, the charge curves of MnO_2–Co^{2+}ad and $Co_{1.4}Mn_{1.6}O_4$ electrodes were almost symmetric to their corresponding discharge counterparts with a slight curvature, indicating the pseudocapacitive contribution along with the double layer contribution. According to the following equation

$$C_s = I \times \Delta t/(\Delta V \times m) \quad (4)$$

where I is the constant discharge current, t is the discharge time, V is the potential drop during discharge, the C_s values of MnO_2–Co^{2+}ad, $Co_{1.4}Mn_{1.6}O_4$ and MnO_2 nanowires can be

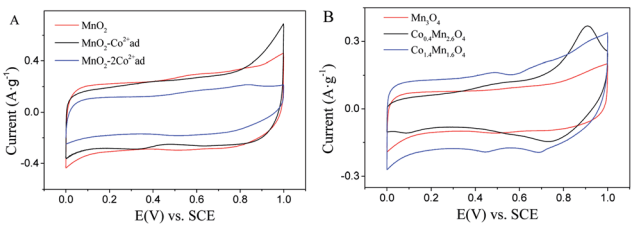

Fig. 5 CVs of (A) MnO_2–xCo^{2+}ad and (B) $Co_xMn_{3-x}O_4$ at 5 mV s^{-1} in 1 M Na_2SO_4 solution.

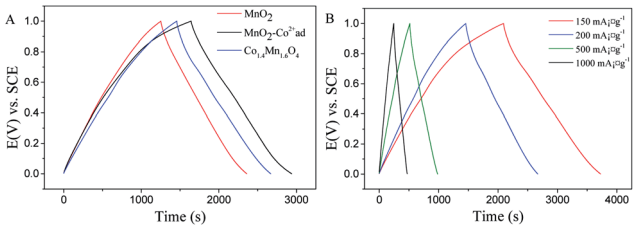

Fig. 6 Galvanostatic charge/discharge curves of (A) MnO_2, MnO_2–Co^{2+}ad ions, and $Co_{1.4}Mn_{1.6}O_4$ at 200 mA g^{-1} and (B) $Co_{1.4}Mn_{1.6}O_4$ at 150, 200, 500, 1000 mA g^{-1}.

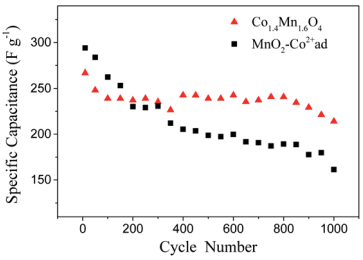

Fig. 8 Cycle life of MnO_2–Co^{2+}ad and $Co_{1.4}Mn_{1.6}O_4$ at 200 mA g^{-1} in 1 M Na_2SO_4 solution.

calculated as 294, 266.84, and 236 F g^{-1} from the discharge curves, respectively, which is consistent with the order indicated by the CVs. In addition, C_s values of $Co_{1.4}Mn_{1.6}O_4$ calculated at 150, 200, 500, and 1000 mA g^{-1} were 279.405, 266.84, 245.35, and 235.2 F g^{-1}, respectively (Fig. 6B), which indicates that about 84.1% of C_s was retained when the current density increased from 150 to 1000 mA g^{-1}. This sound high power performance should be ascribed to the interior geometry and shell functionality of the hollow structure, which increased the contact area between the electrolyte and the active material, and reduced transport lengths for both mass and charge transport. As a result, the diffusion of ions from the electrolyte could gain full access to the available pores of the electrode, leading to an almost complete insertion reaction, and therefore higher C_s.

The galvanostatic charge/discharge measurements proved that $Co_{1.4}Mn_{1.6}O_4$ hollow octahedrons possess good performance despite the decreasing trend when charge current increased to 1000 from 150 mA g^{-1}. To explore the potential for practical application, the current density was further increased to 5000 mA g^{-1} (Fig. 7). The C_s values of $Co_{1.4}Mn_{1.6}O_4$ can be calculated as 235.2, 232.848, 232.848, 310.464, 237.352 F g^{-1} corresponding to the current densities of 1000, 2000, 3000, 4000, 5000 mA g^{-1}, respectively. The capacitances at 2000 and 3000 mA g^{-1} are almost the same as that at 1000 mA g^{-1}, indicating a very stable performance within a wide current range. The large C_s value of 310.464 F g^{-1} at 4000 mA g^{-1} and 237.352 F g^{-1} at 5000 mA g^{-1} represent a quite good high current performance for practical demands.

The capacitance stability of $Co_{1.4}Mn_{1.6}O_4$ and MnO_2–Co^{2+}ad was investigated in the range of 0–1 V at 200 mA g^{-1} in 1 M Na_2SO_4 aqueous solution (Fig. 8). The $Co_{1.4}Mn_{1.6}O_4$ electrode retained about 80.214% (214.043 F g^{-1}) of the initial capacitance after 1000 cycles, while that of MnO_2–Co^{2+}ad retained only about 54.87% (161.319 F g^{-1}). In addition to the intrinsic electrochemical stability of the double-layer, we attribute the much enhanced long-time stability to the following points. On the one hand, such porous hollow texture combines macroporous cores, mesoporous walls, and micropores together, as shown in Fig. 3. The physicochemical properties of the electrolyte in the macropores are similar to those of the bulk electrolyte with the lowest resistance. Ion-buffering reservoirs can be formed in the macropores to minimize the diffusion distances to the interior surfaces. The porous walls provide low-resistant pathways for the ions through the porous particles, and the micropores strengthen the electric double-layer capacitance. On the other hand, the doped cobalt ions can enhance the electric conductivity, which helps us to overcome the primary kinetic limits of electrochemical processes in oxide electrodes.

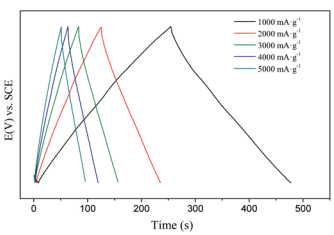

Fig. 7 Galvanostatic charge/discharge curves of $Co_{1.4}Mn_{1.6}O_4$ at 1000, 2000, 3000, 4000 and 5000 mA g^{-1}.

Conclusions

We demonstrated that MnO_2 nanowires, $Co_xMn_{3-x}O_4$ nanorods and hollow octahedrons could be fabricated through a simple hydrothermal method without using any template or surfactant. A dissolution–recrystallization mechanism has been proposed to explain the phase transformation from a MnO_2 nanowire precursor, and the Kirkendall effect to account for the formation of hollow-structured mixed oxides. Improved specific capacitance and good cycle stability were observed in aqueous electrolytes. We believe that the sound high-power capacitance and long-term stability should be ascribed to both the intrinsic low-resistant pathways for the ions through the porous particles, as well as the enhanced electric conductivity, to overcome the primary kinetic limits of electrochemical processes in oxide electrodes. We think that this concept can be extended for enhancing the performance of different electrochemical systems.

Acknowledgements

We thank the financial support from the National Natural Science Foundation of China (NSFC no. 21173017, 51272011 and 21275102), the Program for New Century Excellent Talents in University (NCET-12-0610), and the science and technology research projects from the education ministry (213002A),

National "Twelfth Five-Year" Plan for Science & Technology Support (no. 2011BAZ01B06), Project of Thousand Talents of Chinese High-levelled Talents and the Knowledge Innovation Program of the Chinese Academy of Science (Grant no. KJCX2-YW-M13).

Notes and references

1 G. Wang, L. Zhang and J. Zhang, *Chem. Soc. Rev.*, 2012, **41**, 797.
2 Z. Yu, B. Duong, D. Abbitt and J. Thomas, *Adv. Mater.*, 2013, **25**, 3302–3306.
3 C. Zhou, Y. Zhang, Y. Li and J. Liu, *Nano Lett.*, 2013, **13**, 2078–2085.
4 L.-Q. Mai, F. Yang, Y.-L. Zhao, X. Xu, L. Xu and Y.-Z. Luo, *Nat. Commun.*, 2011, **2**, 381.
5 G. Yu, L. Hu, N. Liu, H. Wang, M. Vosgueritchian, Y. Yang, Y. Cui and Z. Bao, *Nano Lett.*, 2011, **11**, 4438–4442.
6 X. Lu, G. Wang, T. Zhai, M. Yu, S. Xie, Y. Ling, C. Liang, Y. Tong and Y. Li, *Nano Lett.*, 2012, **12**, 5376–5381.
7 X. Lu, M. Yu, T. Zhai, G. Wang, S. Xie, T. Liu, C. Liang, Y. Tong and Y. Li, *Nano Lett.*, 2013, **13**, 2628–2633.
8 H. Jiang, T. Zhao, C. Y. Yan, J. Ma and C. Z. Li, *Nanoscale*, 2010, **2**, 2195–2198.
9 W. Chen, Z. Fan, L. Gu, X. Bao and C. Wang, *Chem. Commun.*, 2010, **46**, 3905.
10 X. W. Lou, D. Deng, J. Y. Lee, J. Feng and L. A. Archer, *Adv. Mater.*, 2008, **20**, 258–262.
11 X. Tang, Z.-h. Liu, C. Zhang, Z. Yang and Z. Wang, *J. Power Sources*, 2009, **193**, 939–943.
12 X. Wang, X.-L. Wu, Y.-G. Guo, Y. Zhong, X. Cao, Y. Ma and J. Yao, *Adv. Funct. Mater.*, 2010, **20**, 1680–1686.
13 G. Tong, J. Guan and Q. Zhang, *Adv. Funct. Mater.*, 2013, **23**, 2406–2414.
14 J. Kang, A. Hirata, H. J. Qiu, L. Chen, X. Ge, T. Fujita and M. Chen, *Adv. Mater.*, 2014, **26**, 269–272.
15 X. W. Lou, L. A. Archer and Z. Yang, *Adv. Mater.*, 2008, **20**, 3987–4019.
16 M. C. Jing Hu, X. Fang and L. Wu, *Chem. Soc. Rev.*, 2011, **40**, 5472–5491.
17 W. Du, R. Liu, Y. Jiang, Q. Lu, Y. Fan and F. Gao, *J. Power Sources*, 2013, **227**, 101–105.
18 C. H. Zhang, L. Fu, N. Liu, M. H. Liu, Y. Y. Wang and Z. F. Liu, *Adv. Mater.*, 2011, **23**, 1020–1024.
19 Z. R. Tian, W. Tong, J. Y. Wang, N. G. Duan, V. V. Krishnan and S. L. Suib, *Science*, 1997, **276**, 926–930.
20 K. Poeppelmeier, *Science*, 2002, **295**, 1849.
21 W. C. Wang, G. McCool, N. Kapur, G. Yuan, B. Shan, M. Nguyen, U. M. Graham, B. H. Davis, G. Jacobs, K. Cho and X. H. Hao, *Science*, 2012, **337**, 832–835.
22 N. Wang, X. Cao, L. He, W. Zhang, L. Guo, C. P. Chen, R. M. Wang and S. H. Yang, *J. Phys. Chem. C*, 2008, **112**, 365–369.
23 N. Wang, L. Guo, L. He, X. Cao, C. P. Chen, R. M. Wang and S. H. Yang, *Small*, 2007, **3**, 606–610.
24 C. Xia, W. Ning and G. Lin, *Sens. Actuators, B*, 2009, **137**, 710–714.
25 X. Cao, X. L. Cai and N. Wang, *Sens. Actuators, B*, 2011, **160**, 771–776.
26 X. Wang and Y. D. Li, *Chem.–Eur. J.*, 2003, **9**, 300–306.
27 X. Wang and Y. D. Li, *J. Am. Chem. Soc.*, 2002, **124**, 2880–2881.
28 Y. D. Yin, R. M. Rioux, C. K. Erdonmez, S. Hughes, G. A. Somorjai and A. P. Alivisatos, *Science*, 2004, **304**, 711–714.

